Article

Dispersion-assisted high-dimensional photodetector

https://doi.org/10.1038/s41586-024-07398-w

Received: 16 September 2023

Accepted: 9 April 2024

Published online: 15 May 2024

Check for updates

Yandong Fan[1,2,6], Weian Huang[1,2,6], Fei Zhu[1,2,6], Xingsi Liu[3], Chunqi Jin[1,2]✉, Chenzi Guo[1], Yang An[1], Yuri Kivshar[4,5], Cheng-Wei Qiu[3]✉ & Wei Li[1,2]✉

Intensity, polarization and wavelength are intrinsic characteristics of light. Characterizing light with arbitrarily mixed information on polarization and spectrum is in high demand[1–4]. Despite the extensive efforts in the design of polarimeters[5–18] and spectrometers[19–27], concurrently yielding high-dimensional signatures of intensity, polarization and spectrum of the light fields is challenging and typically requires complicated integration of polarization- and/or wavelength-sensitive elements in the space or time domains. Here we demonstrate that simple thin-film interfaces with spatial and frequency dispersion can project and tailor polarization and spectrum responses in the wavevector domain. By this means, high-dimensional light information can be encoded into single-shot imaging and deciphered with the assistance of a deep residual network. To the best of our knowledge, our work not only enables full characterization of light with arbitrarily mixed full-Stokes polarization states across a broadband spectrum with a single device and a single measurement but also presents comparable, if not better, performance than state-of-the-art single-purpose miniaturized polarimeters or spectrometers. Our approach can be readily used as an alignment-free retrofit for the existing imaging platforms, opening up new paths to ultra-compact and high-dimensional photodetection and imaging.

It is of great importance to examine the intensity, polarization and spectrum of light simultaneously[1], because such holistic understanding of the properties of light will enable many critical applications in device miniaturization[1], optical communication, remote sensing[28], chemical and biological characterization[29], and astronomic observation[2], for example. Despite the extensive efforts in the design of polarimeters and spectrometers, it remains challenging to yield concurrently high-dimensional signatures of intensity, polarization and spectrum of the light fields. Existing photodetectors could only measure either spectrum[19–27] or polarization[5–17], at the price of sacrificing or simplifying the rich information of the other. To be more specific, they can either map out the intensity and polarization of light at fixed wavelengths or exhibit the data of intensity and wavelength at uniformed polarization[8,14,18,23,30–34]. Such attempts are pushed to the state-of-the-art capability by recent work[18] that demonstrated full-Stokes polarization detection with two different wavelengths (5 μm and 7.7 μm). But if projected into the three-dimensional parametric coordinate system of intensity, polarization and wavelength, all of the existing works lose a certain degree of freedom and can at best detect certain light fields in which polarization or wavelength is preset at several values, as shown by the sliced sections in Fig. 1a, whereas in ubiquitous scenarios in nature[2–4], a to-be-detected light field may carry arbitrarily varying polarizations and intensities within a broad range of wavelengths, as illustrated by the curved surface in Fig. 1a. That essentially demands establishing a high-dimensional photodetector that can fully characterize the three-dimensional parametric coordinate space and accurately describe any light field (Fig. 1a).

Here we suggest and realize a miniaturized photodetector that can characterize the 400–900-nm broadband spectrum and intensities, along with the full-Stokes arbitrarily varying polarizations across the wavelength within a single measurement. To the best of our knowledge, none of the existing bulky or miniaturized single devices can achieve such high-dimensional information, not to mention detection within a single measurement (see comparison in Supplementary Information Note 1). As shown in Fig. 1b, unlike existing photodetectors that primarily rely on constructing and integrating wavelength- and/or polarization-sensitive elements in space (for example, ref. 22 spatially integrates different photonic crystal structures) or time (for example, ref. 18 changes active gating control and measures hundreds of times) to improve the wavelength/polarization detection ability (detection range and sensitivity), we discovered that spatial dispersion (non-local effects) on frequency-dispersive interfaces can modulate a convergent light field with wavevector-dependent responses, generating varying polarization and spectrum sensitivity in various φ (azimuth angle) and θ (incident angle) channels. Therefore, with a uniform dispersive thin-film architecture, light with all channels of rich polarization-sensitive and spectrum-sensitive information can be mapped in single-shot imaging and the high-dimensional polarization and spectrum information can be deciphered with the assistance of deep residual network (ResNet)[35] reconstruction (Fig. 1c).

[1]GPL Photonics Laboratory, State Key Laboratory of Luminescence Science and Technology, Changchun Institute of Optics, Fine Mechanics and Physics, Chinese Academy of Sciences, Changchun, China. [2]University of Chinese Academy of Sciences, Beijing, China. [3]Department of Electrical and Computer Engineering, National University of Singapore, Singapore, Singapore. [4]Nonlinear Physics Centre, Research School of Physics, Australian National University, Canberra, Australian Capital Territory, Australia. [5]Qingdao Innovation and Development Center, Harbin Engineering University, Qingdao, China. [6]These authors contributed equally: Yandong Fan, Weian Huang, Fei Zhu. ✉e-mail: chunqijin@ciomp.ac.cn; chengwei.qiu@nus.edu.sg; weili1@ciomp.ac.cn

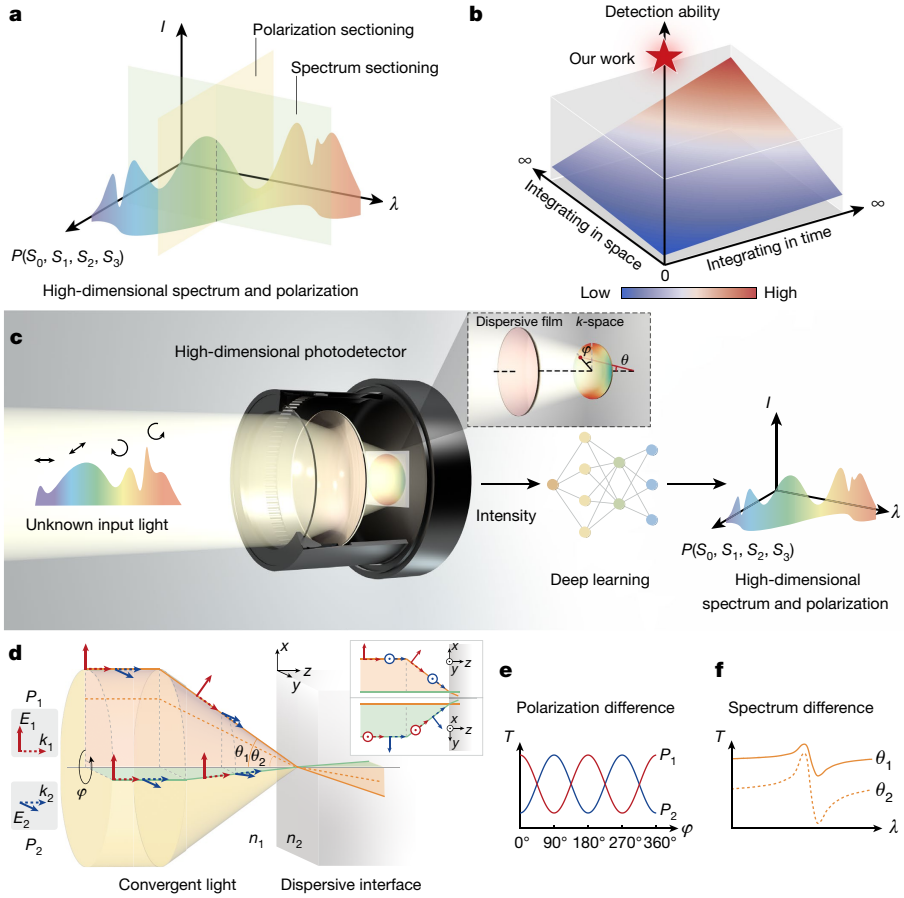

Fig. 1 | Existing approaches versus our high-dimensional photodetector. **a**, Existing photodetection approaches measure, at best, two-dimensional sectioning in the parametric space of intensity, polarization and wavelength, that is, measure the intensity and polarization at fixed wavelengths (light-yellow plane) or measure the intensity and wavelength at uniformed polarization (light-green plane), whereas a light field may carry arbitrarily varying polarizations and intensities within a broad range of wavelengths (curved multicoloured surface). **b**, Unlike existing photodetectors that construct and integrate wavelength- and/or polarization-sensitive elements in space or time to improve the detection ability (range and sensitivity), our approach waives such integration while achieving high-dimensional detection with a single device and single-shot measurement. **c**, In our photodetector, the high-dimensional polarization and spectrum information can be mapped in single-shot imaging and deciphered with a deep residual network. **d**, When light is focused as a convergent beam (yellow cone) and passes through an interface (grey surface), it creates a collection of wavevector channels with various azimuth angles φ and incident angles θ. With a non-zero θ (for example, green ray, $\varphi = -90°$), the orthogonal polarization components of the light, P_1 and P_2, can be differentiated, as P_2 has an electric-field component perpendicular to the interface, whereas the electric field of P_1 remains parallel. By contrast, it is the opposite case when $\varphi = 0°$ (orange ray). These two rays are projected onto the x–z (top inset) and y–z (bottom inset) planes for clarity. **e**, Therefore, the transmission of P_1 (red line) and P_2 (blue line) along the azimuth angle φ dimension exhibit a two-fold rotational symmetry sinusoidal-like pattern but 90° out of phase, a useful feature for polarization discrimination. **f**, When the interface is dispersive, assisted by spatial dispersion, the transmissive/reflective spectra at different incident angles θ_1 and θ_2 can be decorrelated for spectrum reconstruction.

Dispersive and non-local[36–38] flat optics do not necessarily require a position-dependent response and so they can be transversely homogeneous. That makes our concept possible to be implemented with widely available optical thin film, which can be manufactured by standardized coating techniques. We further demonstrate that our approach can be readily used as an alignment-free retrofit for the existing imaging platforms, opening up new paths to ultra-compact, high-dimensional photodetectors and imagers.

Design of high-dimensional photodetector

We start by examining the fundamental continuity conditions for electromagnetic waves. An interface formed by two materials with different refractive indices naturally differentiates polarization ($P(\psi, \delta)$, in which ψ and δ represent the angles of the amplitude ratio ($\tan\psi = E_{yo}/E_{xo}$) and phase difference ($\delta = \delta_y - \delta_x$) of the electric field in the x and y directions) of light ($E_i = A[\cos\psi, \sin\psi e^{i\delta}]^T$) with a non-zero wavevector parallel to the interface. In other words, the transmission of two orthogonal polarization components exhibit different spatial dispersion (momentum and incident-angle θ dependency). Consequently, when a convergent light ($E_i = A[\cos\varphi\cos\psi + \sin\varphi\sin\psi e^{i\delta}, -\sin\varphi\cos\psi + \cos\varphi\sin\psi e^{i\delta}]^T$) containing a collection of wavevector channels (various azimuth angle φ and incident angle θ) passes through an interface (Fig. 1d), the transmission of its two orthogonal polarization components (denoted as P_1 ($P(\psi = 0°, \delta = 0)$) and P_2 ($P(\psi = 90°, \delta = 0)$)) along the azimuth angle φ dimension exhibits a two-fold rotational symmetry sinusoidal-like pattern but 90° out of phase (Fig. 1e), a useful feature for polarization discrimination. Moreover, if the interface has frequency dispersion, combined with spatial dispersion (that is, non-local effect and incident-angle θ dependency), the transmissive/reflective spectra (λ) at different incident angle θ can be decorrelated (Fig. 1f and Supplementary Information Note 2), allowing the possibility of spectrum reconstruction[19,22,23]. Therefore, both polarization and spectrum information of light can, in principle, be coded and reconstructed. Mathematically, when a light carrying high-dimensional polarization ($P(\psi, \delta)$) and spectrum (λ) information is focused and passes through

the interface, the transmitted light forms a circular spot intensity distribution I_t of

$$I_t(\psi, \lambda, \theta, \varphi, \eta) = A^2 \times (T_p(\theta, \lambda) \times B(P, \varphi, \eta) + T_s(\theta, \lambda) \times C(P, \varphi, \eta)) \quad (1)$$

in which A is the amplitude of the incident electric field E_i, $T_p(\theta, \lambda)$ and $T_s(\theta, \lambda)$ are the amplitudes of the transmission spectra for p and s components at a given incident angle and η represents the phase delays of the p and s components of the media. $B(P, \varphi, \eta) = \cos^2\psi\cos^2\varphi + \sin^2\psi\sin^2\varphi + 1/2\sin2\psi\sin2\varphi\cos(\delta + \eta)$ (equation (2)) and $C(P, \varphi, \eta) = \sin^2\psi\cos^2\varphi + \cos^2\psi\sin^2\varphi - 1/2\sin2\psi\sin2\varphi\cos(\delta + \eta)$ (equation (3)) are coefficients determined by the alignment between polarization ($P(\psi, \delta)$) and azimuth (φ) angles, as well as the phase delay (η). Here η is zero for isotropic media (detailed analysis in Supplementary Information Note 3). It can be found that the transmitted light naturally encodes linear polarization and spectrum sensitivity in the φ and θ dimensions, respectively (see Supplementary Information Note 3), with unique dependences (see Supplementary Information Note 4).

Moreover, this sensitivity can be easily engineered and amplified by resonances. To show this, we first construct a Fabry–Pérot cavity with dual roles: (1) for polarization detection, the cavity length can be engineered to maximize the polarization differentiation at a given wavelength in one channel of θ (Fig. 2a). This enhanced polarization differentiation exhibits broadband nature spanning a range of θ channels (Fig. 2b), as the effective cavity length varies with θ; (2) for spectrum detection, the cavity increases the effective frequency dispersion of the interfaces and spatial dispersion (non-locality) owing to wavelength-dependent resonance and multiple interferences, respectively. The transmission spectra at various θ channels can therefore be largely decorrelated (Fig. 2c). Numerically, such a facile design provides strong linear polarization sensitivity (<0.2°) and spectral resolution (<1 nm), respectively (Supplementary Information Note 5).

In that design, because of a phase delay (η) of zero between p and s polarization states in isotropic media, the circular polarization (CP) states cannot be differentiated ($\delta = \pi/2$, $\cos(\delta + \eta) = 0$ in equations (2) and (3)). To further enable circular and full-Stokes polarization detection, we unlock the degree of freedom in phase delay (η) (Supplementary Information Note 3). This can be done by using anisotropic media either in the film[39–41] or in the substrate. Here we consider the simpler case with a mature configuration of commercial waveplate as the substrate (Methods) and show that a $\pi/2$ or $3\pi/2$ phase delay maximizes the CP differentiation $|T_{LCP} - T_{RCP}|$ ($\cos(\delta + \eta) = 1$ in equations (2) and (3)) (Fig. 2d and Supplementary Information Note 3). As such, full-Stokes polarization and broadband spectrum sensitivity can be achieved (Supplementary Information Note 6) and further magnified by stacking multilayer films on both sides of the substrate (Fig. 2e,f; see design process in Supplementary Information Note 7). Notably, such multilayer configuration enables CP differentiation down to a small θ of about 15° (indicating that $|T_{LCP} - T_{RCP}|$ across the broadband range are all higher than 0.1) (Fig. 2e), a useful feature for practical implementation with low numerical aperture (NA) lens or microlens. Moreover, the multilayers create richer spectral features and enhanced non-locality through numerous interferences, which further magnifies the spectral sensitivity (Fig. 2f and Supplementary Information Note 8). Assisted by ResNet (see Methods), our design can numerically achieve average reconstruction errors ($\Delta S_i/S_i = \left(\sum_{m=1}^{N} |(S_{iR} - S_i)/S_i|\right)/N$, in which $i = 1, 2, 3, \ldots, N$ is the number of data points and S_i and S_{iR} are the ground value and the reconstruction Stokes parameter, respectively) of $\Delta S_1/S_1 = 0.93\%$, $\Delta S_2/S_2 = 0.81\%$ and $\Delta S_3/S_3 = 0.85\%$ for full-Stokes polarization detection (Fig. 2g), a spectral resolution of 0.75 nm (LCP) (Supplementary Information Note 9) and a broadband spectrum (400–900 nm, LCP) detection with a reconstruction error of $\varepsilon_\lambda = 1.26\%$ ($\varepsilon_\lambda = ||\lambda_0 - \lambda_R||_1/||\lambda_0||_1$), in which λ_0 and λ_R are the ground value and the reconstructed spectrum, respectively (Fig. 2h). Remarkably, for an unknown incident light with high-dimensional information, further calculations show that its complex broadband spectrum with several arbitrary full-Stokes polarization states can be simultaneously reconstructed with high accuracy ($\Delta S_1/S_1 = 8.41\%$, $\Delta S_2/S_2 = 9.13\%$, $\Delta S_3/S_3 = 4.6\%$ for polarization and $\varepsilon_\lambda = 2.33\%$ for spectrum) (Fig. 2i), highlighting the potential of high-dimensional information detection. More details on datasets and reconstruction can be found in Supplementary Information Note 9.

Intelligent detection of polarization and spectrum

To validate our concept, first we investigate its detection ability of polarization and spectrum, respectively. We experimentally characterize the k-space transmission mappings of various polarization and spectrum states using a back-focal-plane imaging setup (Fig. 3a; see details of the fabrication and setup in Methods) and the mapping results (Supplementary Information Note 10) show reasonable agreement with the calculation. To decipher the Stokes parameters and wavelengths from the mappings (multi-output regression task), we implement a convolutional neural network. Specifically, we modify the ResNet-18 model[35] by replacing the activation function in the output layer with tanh instead of softmax (Fig. 3b; Methods). The images encoded with various polarizations and spectra are used as the dataset. After training, the full-Stokes polarization states under 532 nm obtained by the commercial polarimeter (black circle in Fig. 3c) and our modified ResNet-18 (yellow sphere in Fig. 3c) show errors as low as $\Delta S_1/S_1 = 7.74\%$, $\Delta S_2/S_2 = 3.52\%$ and $\Delta S_3/S_3 = 6.36\%$. This detection accuracy is even comparable to the state-of-the-art miniaturized single-purpose full-Stokes polarimeters (see comparison in Supplementary Information Note 11 and Supplementary Table 2). Also, a set of single-peak spectra under LCP is reconstructed across 460–900 nm and shows an average error of $\varepsilon_\lambda = 0.43\%$ (Fig. 3d). Further, a multi-peak broadband spectrum under LCP is reconstructed within the range 535–625 nm (blue line in Fig. 3e), which agrees well with the reference spectrum measured from a commercial spectrometer (dashed black line in Fig. 3e), with reconstruction error $\varepsilon_\lambda = 5.85\%$. To validate the spectral resolution, two mixed narrowband spectra under LCP are resolved, with peaks separated by 2.7 nm (Fig. 3f and Supplementary Information Note 11). The spectral resolution and reconstruction errors are also comparable to the state-of-the-art miniaturized single-purpose spectrometers (see comparison in Supplementary Information Note 11 and Supplementary Table 3). Therefore, even just working as a single-purpose miniaturized polarimeter or spectrometer, our approach already achieves performance among the best but presents much broader functionalities and substantial room for improvement.

High-dimensional photodetector and imager

Building on the aforementioned capability of full-Stokes polarization and broadband spectrum detection, we now demonstrate a high-dimensional photodetector for characterizing arbitrarily varying polarization states across multi-peak broadband spectrum. As a proof of concept, we consider two scenarios (Fig. 4a–f) in which the sophisticated high-dimensional information cannot be accurately detected by commercial bulky spectrometer and polarimeter. The first scenario considers a two-colour laser field. Here we use a 580 nm (linear polarization) and 635 nm (CP) laser field as an input to our high-dimensional photodetector as well as the reference commercial spectrometer and polarimeter, respectively. In this case, unlike the synthetic polarization from the same frequency, the synthetic polarization from a two-colour laser field is an ultrafast time-varying one (inset Poincaré sphere of Fig. 4a; see calculations in Supplementary Information Note 12) and therefore fundamentally cannot be assigned to a single polarization state. Consequently, the measurements from the commercial polarimeter and spectrometer give inaccurate results in reconstructing the high-dimensional information.

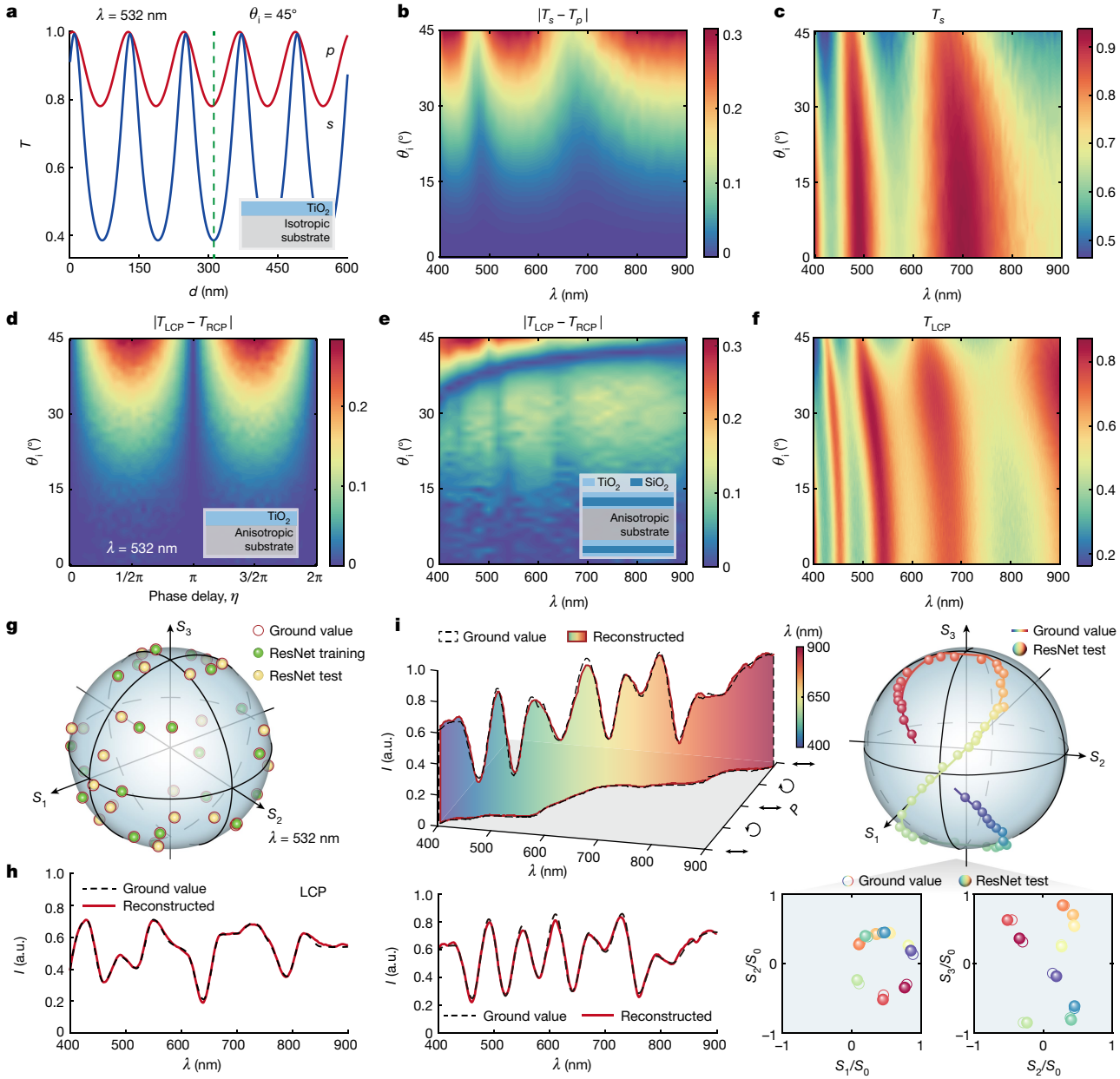

Fig. 2 | Design of our high-dimensional photodetector. a–**c**, Single-layer TiO_2 film is engineered to enlarge linear polarization differentiation at a given wavelength and can further enhance differentiation across a broadband spectrum while enhancing broadband spectrum sensitivity with spanning of θ channels. **a**, Calculated transmission of *p*/*s*-polarized light versus thickness of TiO_2 film at a given wavelength of 532 nm, in the channel of $\theta = 45°$; a thickness of 311 nm is chosen to maximize the transmission difference. **b**, Calculated linear polarization differentiation ($|T_s - T_p|$) versus θ across 400–900 nm. **c**, Calculated transmission spectrum versus θ across 400–900 nm, at a given polarization state. **d**, Phase delay, η, is induced by an anisotropic substrate to enable CP differentiation. The calculated CP differentiation reaches a maximum when $\eta = \pi/2$ or $3\pi/2$. **e**,**f**, Further stacking of multilayer films can enhance CP differentiation to a smaller range of θ channels and broadband spectrum sensitivity. The calculated CP differentiation versus θ across 400–900 nm is shown in **e** and the calculated transmission spectrum versus θ under given LCP is shown in **f**. **g**,**h**, Assisted by ResNet (see Methods), the design is implemented to reconstruct full-Stokes polarization (**g**) and a broadband spectrum (**h**). **i**, Furthermore, a high-dimensional light field with a complex broadband spectrum and several arbitrary full-Stokes polarization states is simultaneously reconstructed. The positions of the continuously changing polarization states are shown on the Poincaré sphere (inset on the right). The high-dimensional reconstruction results are projected onto the spectrum (bottom-left inset) and polarization S_1–S_2 and S_2–S_3 (bottom-right inset) planes for clarity and error analysis. The coloured spheres represent the reconstruction polarization states at selected representative wavelengths (400, 455, 510, 565, 620, 675, 730, 785, 840 and 895 nm). a.u., arbitrary units.

By contrast, our photodetector shows good reconstruction with low average errors of 7.14% (for spectrum; Fig. 4b) and 4.42%, 1.45%, 21.57% (580 nm) and 12.27%, 12.58%, 1.26% (635 nm) (for polarization; Fig. 4c). Such high-dimensional detection can be extended to arbitrary combinations of polarization states covering the entire Poincaré sphere (Supplementary Information Note 13). More details on the experimental setup, datasets and reconstruction can be found in Supplementary Information Note 14.

The second scenario considers the reflection from dispersive interfaces on oblique illumination, which commonly exists in nature. Here an unpolarized, multi-peak broadband light across 485–605 nm is incident on a gold surface with the angle of 45° (Fig. 4d), so the reflected

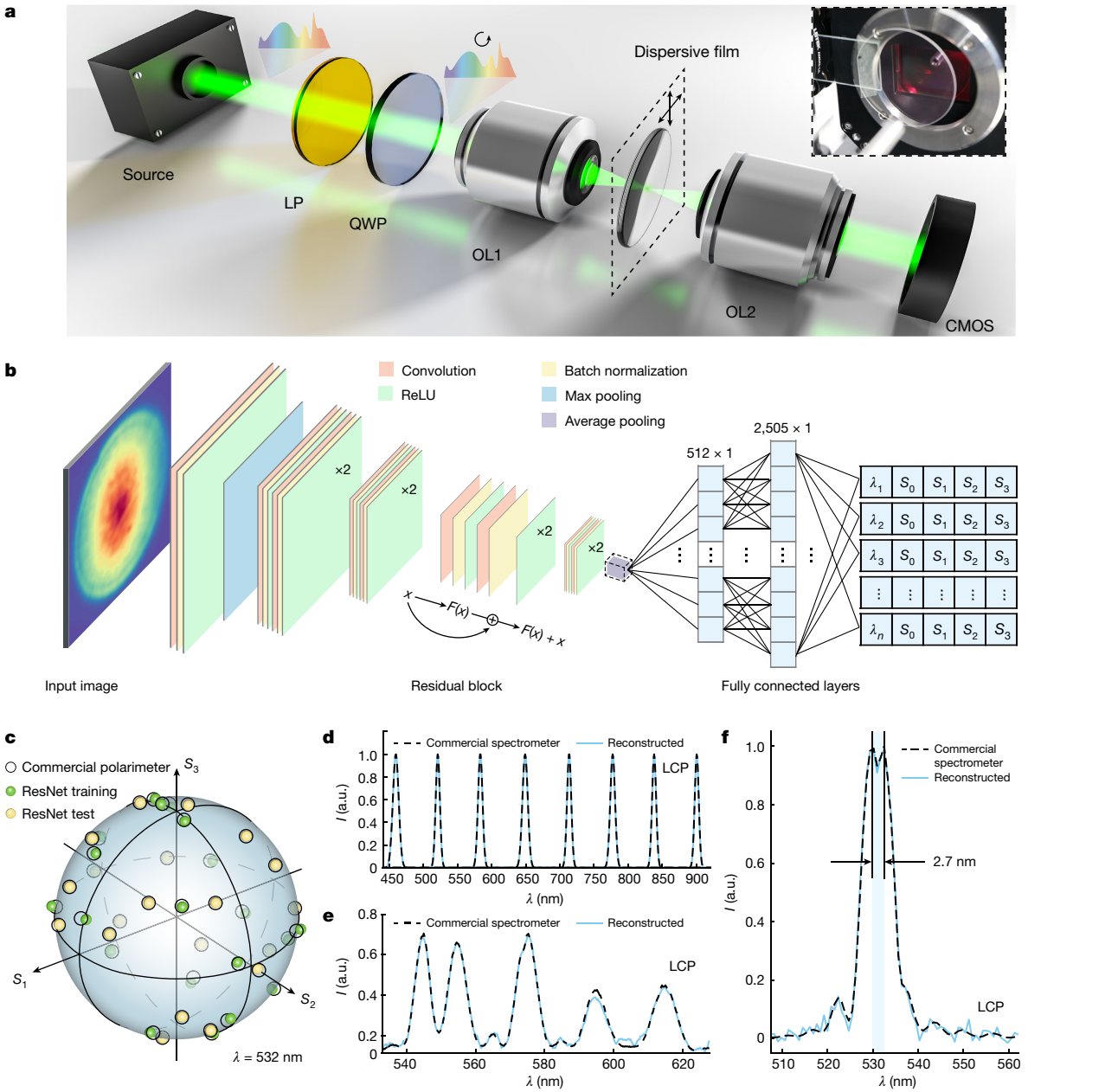

Fig. 3 | Intelligent detection of polarization and spectrum. a, Experimental setup of back-focal-plane imaging: supercontinuum light source coupled with an acoustic-optical tunable filter controls the spectrum of the incident light; the linear polarizer (LP) and a quarter-wave plate (QWP) control the polarization states of the incident light; the objectives (OL1 and OL2) introduce and collect light with various incident and azimuth angles; and the CMOS camera is used to image the back focal plane. Inset, a two-inch sample is attached to a CMOS camera. **b**, Schematic of the modified ResNet-18 model. Input layer: *k*-space transmission mappings; hidden layers: several overlapping interleaved residual blocks help avoid vanishing gradient and degradation; output layer: a 2,505 (501 × 5) matrix of high-dimensional information of the wavelengths ($\lambda_1, \lambda_2, \ldots, \lambda_n$) from 400 nm to 900 nm and four Stokes parameters (S_0, S_1, S_2, S_3) at each wavelength. **c**, Polarization states from the training set (green spheres), the commercial polarimeter (black circles) and our modified ResNet-18 model (yellow spheres) are plotted on the Poincaré sphere, with reconstruction errors of $\Delta S_1/S_1 = 7.74\%$, $\Delta S_2/S_2 = 3.52\%$ and $\Delta S_3/S_3 = 6.36\%$ under 532-nm incident light. All of the Stokes parameters are normalized by the power S_0 for clarity. **d**, Prediction of a set of single-peak spectra under LCP across 460–900 nm (blue line), with a reconstruction error of $\varepsilon_\lambda = 0.43\%$ from a commercial spectrometer (dashed black line). **e**, Prediction of a multi-peak broadband spectrum under LCP in the range 535–625 nm (blue line), with a reconstruction error of $\varepsilon_\lambda = 5.85\%$ from a commercial spectrometer (dashed black line). **f**, Two mixed narrowband spectra under LCP, with peaks separated by 2.7 nm, are experimentally resolved by our high-dimensional photodetector (blue line). a.u., arbitrary units; ReLU, rectified linear unit.

light carries varying ratio of polarization (ROP = $R_s/(R_s + R_p)$) along wavelengths (Supplementary Information Note 15), in which R_s and R_p are the reflected light intensity of *s* and *p* polarization components, respectively. As shown in Fig. 4d, our photodetector can accurately reconstruct the high-dimensional signature, with low average errors of 18.79% (for spectrum; Fig. 4e) and 1.47% (for polarization; Fig. 4f). By contrast, the measurements from the commercial polarimeter and spectrometer cannot observe such a signature. More details on the experimental setup, datasets and reconstruction can be found in Supplementary Information Note 16.

Our approach is readily applicable for imaging, with compact, alignment-free, single-shot acquiring and high-dimensional

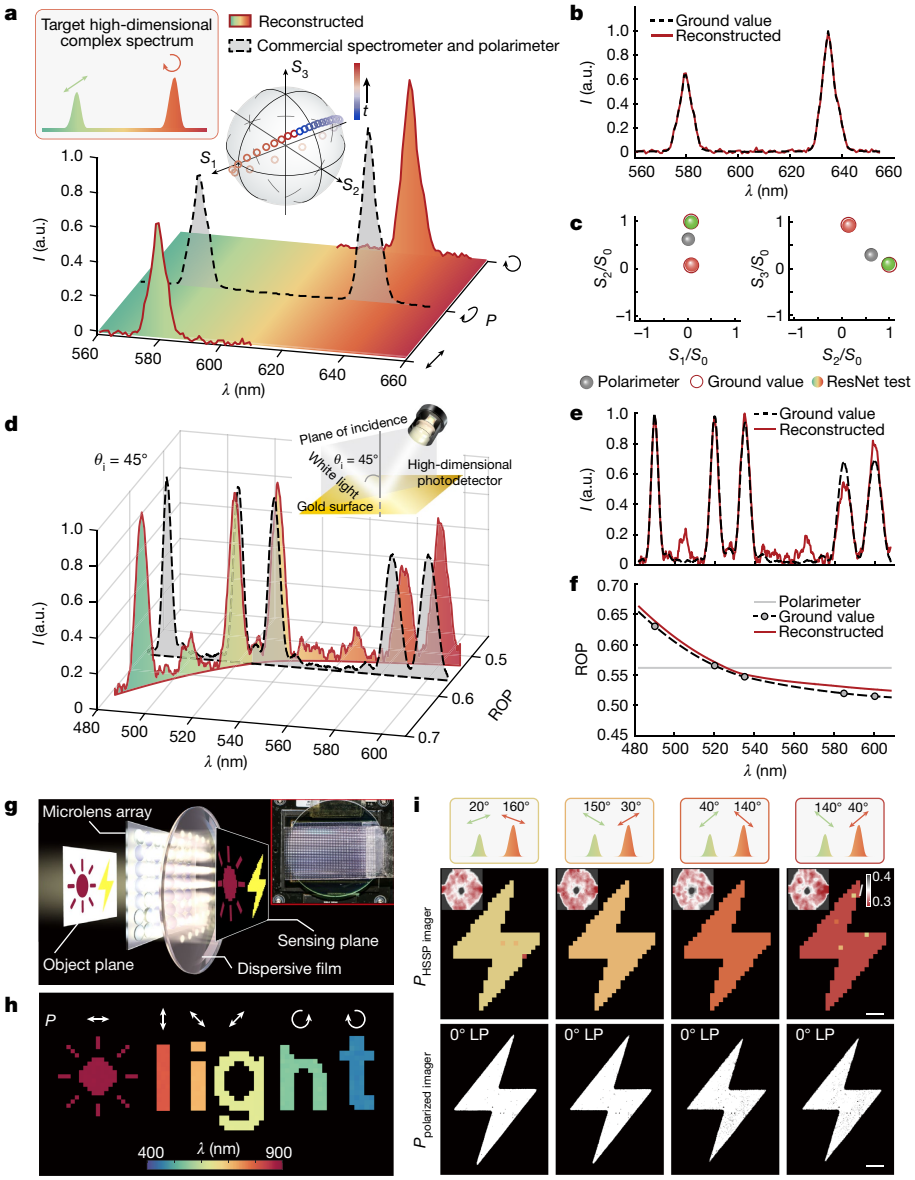

Fig. 4 | High-dimensional photodetector and imager. a–**c**, Detection of two-colour laser field of 580 nm (45° linear polarization) and 635 nm (LCP). The results in **a** are projected onto the spectrum (**b**) and polarization S_1–S_2 and S_2–S_3 (**c**) planes for clarity. Compared with ground values (dashed line and red circles in **b** and **c**, respectively), our photodetector can detect a high-dimensional field (solid line in **a** and **b**, coloured spheres in **c**, green for 580 nm and red for 635 nm), whereas the commercial polarimeter and spectrometer cannot (dashed lines and grey shading in **a** and grey spheres in **c**). **d**–**f**, Detection of the reflected light from the gold surface following unpolarized multi-peak light illumination. The results in **d** are projected onto the spectrum (**e**) and polarization (**f**) planes for clarity. Compared with ground values (dashed lines in **e** and grey circles in **f**), our photodetector can reconstruct the high-dimensional signature, whereas the commercial polarimeter and spectrometer cannot (dashed lines and grey shading in **d** and grey line in **f**). **g**, Schematic of our HSSP imager; inset: photo of imager. **h**, Artificial targets exhibit spatially different polarization and wavelength states: 'sun', horizontally linear polarization, 900 nm; 'l', 90° linear polarization, 810 nm; 'i', 135° linear polarization, 720 nm; 'g', 45° linear polarization, 630 nm; 'h', RCP, 540 nm; 't', LCP, 460 nm. Such features can be recorded by the HSSP imager, with the variance of the polarization and spectrum represented by arrows and colours (see full results in Supplementary Fig. 22). **i**, High-dimensional imaging ($P_{HSSP\ imager}$), for which the HSSP imager can distinguish various high-dimensional light fields (two-colour field with different combinations of polarizations), spatially distributed as a lightning symbol. The insets show the representative raw transmitted intensity distribution from a microlens superpixel. By contrast, a reference full-Stokes polarized imager measures a false linear horizontal polarization for all inputs. Scale bars, 3 mm. a.u., arbitrary units.

capabilities. As a proof of concept, we demonstrate an ultra-compact high-dimensional spatial spectral polarization (HSSP) imager (Fig. 4g) by simply sandwiching our non-local films with a commercially available microlens array (NA = 0.3) and image sensor array (Methods). Each microlens, creating the desired angular channels, serves as a superpixel in the HSSP imager. Here we examine artificial targets (Fig. 4h) with the shapes of the 'sun' and the word 'light', while the targets exhibit spatially different polarization and wavelength states. Such spatially varying features can be recorded by our HSSP imager, as shown in Fig. 4h, thus highlighting its broad spectrum and full-Stokes polarization coverage. More details on the fabrication of the target, datasets, reconstruction, full spectrum and polarization imaging results can be found in Supplementary Information Note 17.

Furthermore, we construct a series of high-dimensional light inputs (a two-colour laser field of 580 nm and 635 nm, with different combinations of polarizations) to our HSSP imager, as well as a reference

imager with a conventional full-Stokes polarized imaging configuration (rotating waveplate and polarizer in front of an imager). The variation between different inputs cannot be detected by the reference imager, whereas they were clearly distinguished by our HSSP imager (Fig. 4i; see detailed analysis and experimental setup in Supplementary Information Note 18).

Summary and outlook

We have demonstrated a non-local high-dimensional photodetector that can decipher arbitrary polarization states and spectrum information from a complex light field with high resolution. Combined with commercially available microlens and sensor arrays, our approach can be readily applicable as a compact, alignment-free and single-shot acquiring imager. It can also be integrated with metalens and the cover glass of image sensors with an ultra-compact form factor.

Although the demonstrations are conducted within 400–900 nm, this spectrum range is not intrinsically limited by our design but by the light source and image sensor array. Our approach only requests a standardized coating process, whereas its non-locality waives transverse inhomogeneity but takes advantage of longitudinally inhomogeneous design freedom. Therefore, our approach in tandem fashion naturally exhibits inherent ultra-broadband potential, free from the integration of polarization- and/or wavelength-sensitive elements in the space or time domains. Our calculations in Supplementary Information Note 19 showcase the ultra-broadband photodetection potential from 400 nm to 10 μm.

We also note that, as well as thin-film schemes, our approach can be further implemented with photonic crystals[42], metasurfaces[43,44], two-dimensional materials[45] and twisted photonic systems[46], which can further markedly enhance the detection resolution. Moreover, with the capability of tuning wavevector domain responses, our approach may further integrate the capabilities of non-local spatial compression, edge detection and distance ranging, towards higher-dimensional detection[1].

Online content

Any methods, additional references, Nature Portfolio reporting summaries, source data, extended data, supplementary information, acknowledgements, peer review information; details of author contributions and competing interests; and statements of data and code availability are available at https://doi.org/10.1038/s41586-024-07398-w.

1. Yuan, S. et al. Geometric deep optical sensing. *Science* **379**, eade1220 (2023).
2. Liodakis, I. et al. Polarized blazar X-rays imply particle acceleration in shocks. *Nature* **611**, 677–681 (2022).
3. Kokhanovsky, A. A. *Light Scattering Reviews* (Springer, 2016).
4. Shaw, J. A. Degree of linear polarization in spectral radiances from water-viewing infrared radiometers. *Appl. Opt.* **38**, 3157–3165 (1999).
5. Li, W. et al. Circularly polarized light detection with hot electrons in chiral plasmonic metamaterials. *Nat. Commun.* **6**, 8379 (2015).
6. Pors, A., Nielsen, M. G. & Bozhevolnyi, S. I. Plasmonic metagratings for simultaneous determination of Stokes parameters. *Optica* **2**, 716–723 (2015).
7. Jung, M. et al. Polarimetry using graphene-integrated anisotropic metasurfaces. *ACS Photonics* **5**, 4283–4288 (2018).
8. Rubin, N. A. et al. Matrix Fourier optics enables a compact full-Stokes polarization camera. *Science* **365**, eaax1839 (2019).
9. Wei, J. et al. Zero-bias mid-infrared graphene photodetectors with bulk photoresponse and calibration-free polarization detection. *Nat. Commun.* **11**, 6404 (2020).
10. Wei, J., Xu, C., Dong, B., Qiu, C.-W. & Lee, C. Mid-infrared semimetal polarization detectors with configurable polarity transition. *Nat. Photon.* **15**, 614–621 (2021).
11. Fang, C., Li, J., Zhou, B. & Li, D. Self-powered filterless on-chip full-Stokes polarimeter. *Nano Lett.* **21**, 6156–6162 (2021).
12. Dai, M. et al. On-chip mid-infrared photothermoelectric detectors for full-Stokes detection. *Nat. Commun.* **13**, 4560 (2022).
13. Rubin, N. A. et al. Imaging polarimetry through metasurface polarization gratings. *Opt. Express* **30**, 9389–9412 (2022).
14. Song, I. et al. Helical polymers for dissymmetric circularly polarized light imaging. *Nature* **617**, 92–99 (2023).
15. Wei, J. et al. Geometric filterless photodetectors for mid-infrared spin light. *Nat. Photon.* **17**, 171–178 (2023).
16. Wan, L. et al. Sensitive near-infrared circularly polarized light detection via non-fullerene acceptor blends. *Nat. Photon.* **17**, 649–655 (2023).
17. Li, L. W., Rubin, N. A., Juhl, M., Park, J.-S. & Capasso, F. Evaluation and characterization of imaging polarimetry through metasurface polarization gratings. *Appl. Opt.* **62**, 1704–1722 (2023).
18. Ma, C. et al. Intelligent infrared sensing enabled by tunable moiré quantum geometry. *Nature* **604**, 266–272 (2022).
19. Bao, J. & Bawendi, M. G. A colloidal quantum dot spectrometer. *Nature* **523**, 67–70 (2015).
20. Tittl, A. et al. Imaging-based molecular barcoding with pixelated dielectric metasurfaces. *Science* **360**, 1105–1109 (2018).
21. Yang, Z. et al. Single-nanowire spectrometers. *Science* **365**, 1017–1020 (2019).
22. Wang, Z. et al. Single-shot on-chip spectral sensors based on photonic crystal slabs. *Nat. Commun.* **10**, 1020 (2019).
23. Yang, Z., Albrow-Owen, T., Cai, W. & Hasan, T. Miniaturization of optical spectrometers. *Science* **371**, eabe0722 (2021).
24. Yuan, S., Naveh, D., Watanabe, K., Taniguchi, T. & Xia, F. A wavelength-scale black phosphorus spectrometer. *Nat. Photon.* **15**, 601–607 (2021).
25. Yoon, H. H. et al. Miniaturized spectrometers with a tunable van der Waals junction. *Science* **378**, 296–299 (2022).
26. Deng, W. et al. Electrically tunable two-dimensional heterojunctions for miniaturized near-infrared spectrometers. *Nat. Commun.* **13**, 4627 (2022).
27. Tua, D. et al. Imaging-based intelligent spectrometer on a plasmonic rainbow chip. *Nat. Commun.* **14**, 1902 (2023).
28. Schweiger, A. K. & Laliberte, E. Plant beta-diversity across biomes captured by imaging spectroscopy. *Nat. Commun.* **13**, 2767 (2022).
29. Chan, W. P. et al. A high-throughput multispectral imaging system for museum specimens. *Commun. Biol.* **5**, 1318 (2022).
30. Shaltout, A., Liu, J., Kildishev, A. & Shalaev, V. Photonic spin Hall effect in gap–plasmon metasurfaces for on-chip chiroptical spectroscopy. *Optica* **2**, 860–863 (2015).
31. Chen, W. T. et al. Integrated plasmonic metasurfaces for spectropolarimetry. *Nanotechnology* **27**, 224002 (2016).
32. Ding, F., Pors, A., Chen, Y., Zenin, V. A., & Bozhevolnyi, S. I. Beam-size-invariant spectropolarimeters using gap-plasmon metasurfaces. *ACS Photonics* **4**, 943–949 (2017).
33. Altaqui, A. et al. Mantis shrimp-inspired organic photodetector for simultaneous hyperspectral and polarimetric imaging. *Sci. Adv.* **7**, eabe3196 (2021).
34. Ni, Y. et al. Computational spectropolarimetry with a tunable liquid crystal metasurface. *eLight* **2**, 23 (2022).
35. He, K., Zhang, X., Ren, S. & Sun, J. in *Proc. 2016 IEEE Conference on Computer Vision and Pattern Recognition (CVPR)* 770–778 (IEEE, 2016).
36. Shastri, K. & Monticone, F. Nonlocal flat optics. *Nat. Photon.* **17**, 36–47 (2022).
37. Silva, A. et al. Performing mathematical operations with metamaterials. *Science* **343**, 160–163 (2014).
38. Song, J.-H., van de Groep, J., Kim, S. J. & Brongersma, M. L. Non-local metasurfaces for spectrally decoupled wavefront manipulation and eye tracking. *Nat. Nanotechnol.* **16**, 1224–1230 (2021).
39. Niu, S. et al. Giant optical anisotropy in a quasi-one-dimensional crystal. *Nat. Photon.* **12**, 392–396 (2018).
40. Biswas, S., Grajower, M. Y., Watanabe, K., Taniguchi, T. & Atwater, H. A. Broadband electro-optic polarization conversion with atomically thin black phosphorus. *Science* **374**, 448–453 (2021).
41. Chen, X. et al. Solution-processed inorganic perovskite crystals as achromatic quarter-wave plates. *Nat. Photon.* **15**, 813–816 (2021).
42. Fan, S. & Joannopoulos, J. D. Analysis of guided resonances in photonic crystal slabs. *Phys. Rev. B* **65**, 235112 (2002).
43. Chen, Y. et al. Observation of intrinsic chiral bound states in the continuum. *Nature* **613**, 474–478 (2023).
44. Cai, G. et al. Compact angle-resolved metasurface spectrometer. *Nat. Mater.* **23**, 71–78 (2024).
45. Kumar, P. et al. Photonically active bowtie nanoassemblies with chirality continuum. *Nature* **615**, 418–424 (2023).
46. Tang, H. et al. Experimental probe of twist angle–dependent band structure of on-chip optical bilayer photonic crystal. *Sci. Adv.* **9**, eadh8498 (2023).

Methods

Numerical calculations

We compute the full-Stokes polarization-dependent and wavelength-dependent responses of our designs based on a 4 × 4 propagation matrix. Specifically, we express the transfer matrix Γ_N for a film comprising i (i = 1, 2, 3,..., N) layers as follows:

$$\Gamma_N = A_0^{-1} T_1 T_2 \ldots T_N A_{N+1}$$

in which A represents the transfer matrix between interfaces, layer 0 represents the incident medium and $N+1$ represents the substrate. T_i represents the transfer matrix of a single layer (Supplementary Information Note 3), which can be defined as:

$$T_i = A_i P_i A_i^{-1}$$

and the 4 × 4 propagation matrix P_i can be written as,

$$P_i = \begin{pmatrix} e^{-i\frac{\omega}{c}q_{i1}d_i} & 0 & 0 & 0 \\ 0 & e^{-i\frac{\omega}{c}q_{i2}d_i} & 0 & 0 \\ 0 & 0 & e^{-i\frac{\omega}{c}q_{i3}d_i} & 0 \\ 0 & 0 & 0 & e^{-i\frac{\omega}{c}q_{i4}d_i} \end{pmatrix}$$

in which q_i represents the dimensionless z component of the wavevector and d_i denotes the thickness of each layer. The frequency and velocity of the light are represented by ω and c, respectively.

In Fig. 2d–f and Supplementary Figs. 7 and 8, we consider an incoherent condition in the calculations, as the anisotropic substrate thickness (500 μm) is far greater than the coherent length (approximately 60 μm) of the light source. This is achieved by introducing a slight variation (a random quantity between −1/10 to +1/10 of the working wavelength) to the thickness d_i of the incoherent layers in each calculation and averaging over 900 calculations.

Sample fabrication

We fabricate three samples including one isotropic sample (Fig. 2a) and two anisotropic samples (Fig. 2e) for high-dimensional information detection (Figs. 3c–f and 4a–f) and imaging (Fig. 4h,i) by ion-assisted deposition. The isotropic sample consists of a layer of TiO_2 with a thickness of 311 nm on a two-inch fused silica substrate with a thickness of 0.5 mm. For the anisotropic sample (Figs. 3c–f and 4a–f and Supplementary Fig. 8), multilayer stacks of TiO_2 and SiO_2 are deposited on both sides of a half-inch commercially available waveplate. The waveplate is composed of α-quartz and MgF_2, with thicknesses of 255.3 μm and 209.4 μm, respectively (details in Supplementary Information Note 7). On the basis of this design, to achieve a larger imaging area in the imaging experiments (Fig. 4h,i), we use a two-inch-diameter waveplate with an extra layer of K9 glass for mechanical support.

Experimental setup

For the experimental characterization (Figs. 3c–f and 4a–f), the input light is generated by a supercontinuum light source (YSL SC-PRO-7) coupled with an acousto-optic tunable filter (YSL AOTF0019). The acousto-optic tunable filter can generate Gaussian-type narrowband light (full width at half maximum of approximately 2–6 nm). By simultaneously activating several channels, it can produce broadband multi-peak light. The linear polarizers and a quarter-wave plate are used to generate arbitrary full-Stokes polarized light (Figs. 3c–f and 4a–c), and a depolarizer is used to produce the unpolarized white light (Fig. 4d–f). Two objectives (OptoSigma EPLE 100×-0.8NA; Mitutoyo Plan Apo Infinity Corrected Long WD Objective 100×-0.7NA) are used to introduce and collect the light with various incident and azimuth angles. Then the k-space transmission mappings can be obtained in the back focal plane of the objective by a CMOS camera (Orion OR-455BSI (Sony IMX455)). The experimental setup used in Figs. 4a–c and 4d–f are detailed in Supplementary Information Notes 14 and 16, respectively.

For imaging experiments (Fig. 4h,i), the setup we demonstrate is an ultra-compact imager. We use a commercially available microlens array to introduce the light with various incident and azimuth angles. The diameter of each microlens is 0.8 mm and the focal length is 1.272 mm. The array consists of 2,720 superpixels with 55 × 32 mm^2 imaging area. The sensing plane is placed away from the focal spot and the distance between the microlens array and the sensing plane along the optical axis is 2.5 mm. More details of the experimental setup can be found in Supplementary Information Notes 17 and 18.

ResNet model and training details

As shown by the schematic of the modified ResNet-18 model in Fig. 3b, the input layer is a mapping matrix measured at arbitrary combinations of polarization and spectrum states. The output layer provides a 5 × n-component vector (predicted values) including n discretized wavelengths ($\lambda_1, \lambda_2, \ldots, \lambda_n$) and four Stokes parameters (S_0, S_1, S_2, S_3) at each wavelength. The output layer is obtained by connecting the tanh function (hyperbolic tangent activation function) in the range from −1 to 1. $S_i = S_i/S_0$ (i = 1, 2, 3) is used to match the value of polarization parameters in the range (−1, 1) and the spectrum is normalized to the range of (0, 1). For the network training, stochastic gradient descent is used to optimize the process, with a momentum of 0.9 and adaptive learning rate scheduling in PyTorch. The computations are executed on an NVIDIA A100 GPU with 40 GB VRAM. Specifically, the detailed reconstruction processes for different information (Figs. 2g–i, 3c–f and 4a–f,h,i) are demonstrated in Supplementary Information Notes 9, 11, 13, 14, 16, 17 and 18.

Data availability

The data that support the plots in this paper are available from the corresponding authors. Source data are provided with this paper.

Code availability

The generic code to generate the original data for all relevant tasks of this study is freely available at https://github.com/WeianHuang23/Dispersion-assisted_High-dimensional_Photodetector.git.

Acknowledgements W.L. and C.J. are supported by the National Natural Science Foundation of China (grant nos. 62134009, 62121005 and 62305328). C.-W.Q. is supported by the Competitive Research Program Award (NRF-CRP22-2019-0006 and CRP30-2023-0035) from the National Research Foundation (NRF), Prime Minister's Office Singapore and by a grant (A-0005947-16-00) from Advanced Research and Technology Innovation Centre (ARTIC), National University of Singapore. C.G. acknowledges the support from CAS Youth Innovation Promotion Association Project (no. 20211214). We thank T. Bai, S. Guo, J. Yang and M. Xiao for helpful discussions.

Author contributions W.L. conceived the project. Y.F., C.J., F.Z. and W.L. performed the theoretical calculations and design. Y.F. performed the measurements. W.H. developed the program for applying the neural network. Y.F., C.J. and Y.A. prepared the samples. W.L., C.J., Y.F., W.H., F.Z., X.L., C.-W.Q. and Y.K. discussed and analysed the results. W.L., C.-W.Q., Y.K., C.J. and C.G. wrote and revised the manuscript. W.L., C.-W.Q. and Y.K. supervised the project.

Competing interests W.L., Y.F., C.J., W.H., F.Z. and C.-W.Q. are inventors of a patent application that covers the concept and implementation of the dispersion-assisted high-dimensional photodetector and its applications. The other authors declare no competing interests.

Additional information

Supplementary information The online version contains supplementary material available at https://doi.org/10.1038/s41586-024-07398-w.

Correspondence and requests for materials should be addressed to Wei Li, Cheng-Wei Qiu or Chunqi Jin.

Peer review information *Nature* thanks the anonymous reviewers for their contribution to the peer review of this work.